

NASA/TM—2015–218997



# Secondary Instability of Stationary Crossflow Vortices in Mach 6 Boundary Layer over a Circular Cone

*Fei Li, Meelan M. Choudhari, and Pedro Paredes-Gonzalez  
Langley Research Center, Hampton, Virginia*

*Lian Duan  
Missouri University of Science and Technology, Rolla, Missouri*

---

**December 2015**

## NASA STI Program ... in Profile

Since its founding, NASA has been dedicated to the advancement of aeronautics and space science. The NASA scientific and technical information (STI) program plays a key part in helping NASA maintain this important role.

The NASA STI program operates under the auspices of the Agency Chief Information Officer. It collects, organizes, provides for archiving, and disseminates NASA's STI. The NASA STI program provides access to the NTRS Registered and its public interface, the NASA Technical Reports Server, thus providing one of the largest collections of aeronautical and space science STI in the world. Results are published in both non-NASA channels and by NASA in the NASA STI Report Series, which includes the following report types:

- **TECHNICAL PUBLICATION.** Reports of completed research or a major significant phase of research that present the results of NASA Programs and include extensive data or theoretical analysis. Includes compilations of significant scientific and technical data and information deemed to be of continuing reference value. NASA counter-part of peer-reviewed formal professional papers but has less stringent limitations on manuscript length and extent of graphic presentations.
- **TECHNICAL MEMORANDUM.** Scientific and technical findings that are preliminary or of specialized interest, e.g., quick release reports, working papers, and bibliographies that contain minimal annotation. Does not contain extensive analysis.
- **CONTRACTOR REPORT.** Scientific and technical findings by NASA-sponsored contractors and grantees.

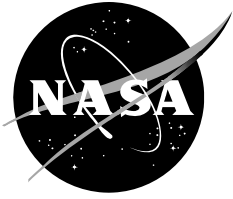
- **CONFERENCE PUBLICATION.** Collected papers from scientific and technical conferences, symposia, seminars, or other meetings sponsored or co-sponsored by NASA.
- **SPECIAL PUBLICATION.** Scientific, technical, or historical information from NASA programs, projects, and missions, often concerned with subjects having substantial public interest.
- **TECHNICAL TRANSLATION.** English-language translations of foreign scientific and technical material pertinent to NASA's mission.

Specialized services also include organizing and publishing research results, distributing specialized research announcements and feeds, providing information desk and personal search support, and enabling data exchange services.

For more information about the NASA STI program, see the following:

- Access the NASA STI program home page at <http://www.sti.nasa.gov>
- E-mail your question to [help@sti.nasa.gov](mailto:help@sti.nasa.gov)
- Phone the NASA STI Information Desk at 757-864-9658
- Write to:  
NASA STI Information Desk  
Mail Stop 148  
NASA Langley Research Center  
Hampton, VA 23681-2199

NASA/TM—2015–218997



# Secondary Instability of Stationary Crossflow Vortices in Mach 6 Boundary Layer over a Circular Cone

*Fei Li, Meelan M. Choudhari, and Pedro Paredes-Gonzalez  
Langley Research Center, Hampton, Virginia*

*Lian Duan  
Missouri University of Science and Technology, Rolla, Missouri*

National Aeronautics and  
Space Administration

*Langley Research Center  
Hampton, VA 23681*

---

**December 2015**

## Acknowledgments

This work was performed as part of the Revolutionary Computational Aerosciences discipline under the Transformational Tools and Technologies project of NASA's Transformative Aeronautics Concepts Program. Computational resources for this work were provided by the NASA High-End Computing (HEC) Program through the NASA Advanced Supercomputing (NAS) Division at Ames Research Center. MC would like to thank Prof. Steven Schneider, Dr. Christopher Ward, and Mr. Joshua Edelman from Purdue University for several technical interactions. Thanks are also due to Prof. William Saric and Mr. Stuart Craig from the Texas A & M University for the hot wire measurements in NASA Langley Mach 6 Quiet Tunnel that helped provide a framework for the present computations. Finally, the authors acknowledge Prof. Pino Martin from the University of Maryland for providing the original version of the DNS code used in this effort.

The use of trademarks or names of manufacturers in this report is for accurate reporting and does not constitute an official endorsement, either expressed or implied, of such products or manufacturers by the National Aeronautics and Space Administration.

Available from:

NASA STI Program / Mail Stop 148  
NASA Langley Research Center  
Hampton, VA 23681-2199  
Fax: 757-864-6500

## **Abstract**

Hypersonic boundary layer flows over a circular cone at moderate incidence can support strong crossflow instability. Due to more efficient excitation of stationary crossflow vortices by surface roughness, such boundary layer flows may transition to turbulence via rapid amplification of the high-frequency secondary instabilities of finite amplitude stationary crossflow vortices. The amplification characteristics of these secondary instabilities are investigated for crossflow vortices generated by an azimuthally periodic array of roughness elements over a 7-degree half-angle circular cone in a Mach 6 free stream. Depending on the local amplitude of the stationary crossflow mode, the most unstable secondary disturbances either originate from the second (i.e., Mack) mode instabilities of the unperturbed boundary layer or correspond to genuine secondary instabilities that reduce to stable disturbances at sufficiently small amplitudes of the stationary crossflow vortex. The predicted frequencies of dominant secondary disturbances are similar to those measured during wind tunnel experiments at Purdue University and the Technical University of Braunschweig, Germany.

## Introduction

By virtue of its influence on surface heat transfer, skin friction, and separation characteristics, boundary layer transition from laminar to turbulent state can have a major impact on the design and performance of hypersonic flight vehicles. Transition over realistic vehicle surfaces is often caused by surface roughness of sufficiently large amplitude. However, when the surface is relatively smooth, the laminar-turbulent transition process is initiated by linear instabilities of the laminar boundary layer. Typically, the second (or Mack) mode instability dominates transition in 2D/axisymmetric boundary layers at hypersonic speeds [1], although centrifugal (i.e., Görtler) instabilities may also come into play when the body surface has concave curvature along the streamwise direction [2]. Three-dimensional boundary layers involve the additional mechanisms of stationary and traveling modes of crossflow instability [3] and, depending on the geometric configuration, the attachment line instability as well.

Regardless of the speed regime, linear stability correlations have been quite successful in predicting the onset of transition when a single instability mechanism dominates the transition process. Mixed mode transition has been more difficult to predict. Furthermore, measurements of crossflow instability in low-speed boundary layers have exposed the shortcomings of applying purely linear predictive models to transition in 3D boundary layers by revealing the importance of nonlinear effects during crossflow dominated transition [3]. The canonical configuration of a circular cone at angle of attack (AOA) includes the necessary elements to study both mixed mode transition and crossflow development in the context of both supersonic [4–12] and hypersonic [13–29] boundary-layer flows. Instability mechanisms for the boundary layer flow over an elliptic cone have been investigated in Refs. [19] and [29]–[46]. While the elliptic cone configuration supports similar instability mechanisms as the circular cone at an angle of incidence, the details of transition patterns can be different as noted in Ref. [41].

The availability of low-disturbance (i.e., quiet) hypersonic facilities opens up the possibility of a detailed study of the above mentioned instability phenomena in a controlled environment [21–25]. However, because of the complexity of the crossflow transition process, the interpretation of wind tunnel measurements must be guided by a detailed computational analysis of the flow field and its stability characteristics. The objective of this ongoing effort is to help provide the required characterization in support of wind tunnel experiments so as to eventually resolve some of the outstanding issues related to transition mechanisms in three-dimensional hypersonic boundary layers over nominally smooth surfaces.

The development of stationary and traveling crossflow instabilities on circular and elliptic cone configurations at a freestream Mach number of 6.0 has been addressed in Refs. [17–29]. Limited measurements of traveling crossflow instability by Borg et al. [47] have yielded encouraging comparison with the linear stability predictions by Li et al. [19]. More recent quiet tunnel experiments indicate that similar comparisons may soon be possible for the stationary crossflow modes as well. In particular, experimental measurements of crossflow instability over a yawed circular cone in two different Mach 6 quiet wind tunnels have been reported recently. Each of these investigations is rather remarkable, albeit for different reasons. Ward et al. [21] performed measurements using temperature sensitive paint (to measure time averaged surface heat transfer) and dynamic surface pressure transducers at a variety of flow conditions ( $\alpha = 3$  deg and 4 deg,  $Re = 9.84 \times 10^6$  to  $12.01 \times 10^6$ , both with and without surface roughness, and a range of axial and azimuthal locations of unsteady pressure sensors) to provide strong evidence of secondary instability. Craig and Saric [25] performed in-depth hot wire measurements of the boundary-layer flow over a selected range of azimuthal locations at a fixed freestream condition. The unsteady pressure spectra measured by Ward et al. [21] in the BAMQT facility at Purdue University showed two major peaks at most of the measurement locations and flow conditions with  $\alpha = 3$  deg and  $\alpha = 4$  deg. The lower-frequency peak near 40 kHz to 50 kHz was attributed to traveling crossflow modes and the higher frequency peak ranging from 125 kHz to 500 kHz (i.e., nearly three to ten times the frequency of the lower peak) was attributed to the secondary instability of stationary crossflow modes. A limited set of wind tunnel runs showed an additional, intermediate-frequency peak near 150 kHz, but the character and the origin of the fluctuations associated with this peak could not be established. Subsequent measurements by McKiernan et al. [22] and Edelman and Schneider [23] extended

the above measurements to  $\alpha = 6$  deg. For a narrower set of sensor locations, the peak frequency of the measured surface pressure spectra was between 300 and 335 kHz. The peak frequency decreased slightly as the sensor location shifted downstream.

The hot wire measurements by Craig and Saric [24, 25] in the NASA Langley Mach 6 Quiet Tunnel at Texas A & M University provided quantitative maps of steady and unsteady mass-flux distributions across the cross-section of the stationary crossflow vortices at selected axial locations within the range of  $X = 0.35$  and  $0.4$  meters and azimuthal locations of  $\phi$  between 112 and 124 degrees relative to the windward plane of symmetry. Similar to the Purdue measurements [21–23], they observed two peaks in the frequency spectra. The low frequency peak over 15 to 60 kHz was approximately consistent with the surface pressure spectra of Ward et al. [21]. However, the high-frequency peak in the unsteady hot wire measurements involved significantly lower frequencies of 80 to 130 kHz. The high-frequency disturbances were concentrated over the inclined shear layer that is visible from the overturning stationary mass-flux contours produced by the finite amplitude stationary crossflow vortices. The measured mode shapes were remarkably similar to the secondary instability mode driven by the azimuthal shear induced by the stationary vortex. According to Craig and Saric [25], the frequency of the azimuthal-shear mode of secondary instability scales like  $2U/\delta$ , which is equal to 120 kHz for the conditions of their measurement. Thus, the frequency range of measured high-frequency disturbances in their experiment was in line with this estimate. Computations by Oliviero et al. [26] indicated qualitative similarities with the stationary crossflow modes measured in Ref. [25]; however, significant quantitative differences were apparent in the disturbance amplitudes as well as mass flux contours.

Conventional facility measurements analogous to the quiet-tunnel measurements at Purdue University have been reported by Munoz et al. [20]. They used infrared measurements of surface temperature to infer heat transfer and surface pressure measurements to infer the frequencies, amplitudes, and wave angles of instability wave packets over a Mach 6 yawed circular cone tested at the Technical University of Braunschweig. The average spatial extensions of these packets were also mapped out using circumferential cross-correlations. For sensors near  $\phi = 90$  deg from the windward ray and  $X$  locations between 0.21 m and 0.36 m, the low frequency lobe was spread over the range between 20 and 50 kHz and the high-frequency peak was centered at approximately 300 kHz to 350 kHz. These frequency values are remarkably similar to those measured under quiet conditions and, therefore, even though Munoz et al. attributed the high-frequency peak to possible second mode instability, it is possible that this peak was actually associated with secondary instabilities of the distorted mean flow in the presence of strong stationary crossflow vortices. At the larger azimuthal angle of 110 deg, Munoz et al. noted higher disturbance amplitudes and slightly reduced center frequency of the high-frequency lobe, analogous to the measurements of Ward et al. [21]. Nonlinear interactions between the low-frequency disturbances (traveling crossflow modes) and the high-frequency disturbances (attributed to second mode perturbations) were also inferred at the most downstream measurement location ( $X = 0.36$  m) by using bicoherence analysis. Analysis of cross-correlations between multiple pressure transducers indicated that the dominant propagation angle associated with the low-frequency disturbances was between 60 and 70 degrees relative to the flow velocity at the edge of the boundary layer.

Computations of secondary instability of crossflow modes in a hypersonic boundary layer were first reported by Li et al. [29]. The predicted secondary instabilities with the highest growth rates had frequencies that were comparable to those measured in the Purdue experiments [21–23], but the computations also revealed the existence of less unstable modes with lower disturbance frequencies that were comparable to those measured by Craig and Saric [25]. The unstable secondary modes were shown to have an intricate variety of modal structure, with fluctuations concentrated in various subregions of high shear associated with the stationary crossflow structures. However, in general, no dominant modes with spatial concentration on the top of the inclined shear layer (the mode shape typically associated with the wall-normal shear of the basic state) were found. However, the analysis of Li et al. [29] was limited to local secondary instability analyses at selected stations and, hence, did not provide any information about the integrated amplification of the secondary

disturbances. The present paper rectifies that shortcoming by tracking the evolution of unstable secondary modes over the region of interest.

The remaining sections of this document are laid out as follows. A brief summary of the flow configuration of interest is given in Section 1, which also describes the analysis codes used in this study. Nonlinear evolution of stationary crossflow modes using direct numerical simulations is described in Section 2.1 and the secondary instability of these finite amplitude crossflow vortices is investigated in Section 2.2. Summary and concluding remarks are presented in Section 3.

## Nomenclature

$f$	=	frequency of instability waves [kHz]
$M_e$	=	boundary-layer edge Mach number
$M_\infty$	=	freestream Mach number
$n$	=	azimuthal wavenumber, i.e., number of waves across circumference
$U$	=	streamwise velocity [m/s]
$U_e$	=	boundary-layer edge velocity [m/s]
$U_\infty$	=	freestream velocity [m/s]
$P_\infty$	=	freestream pressure [Pa]
r.m.s.	=	root mean square
$Re$	=	freestream unit Reynolds number [ $m^{-1}$ ]
$s$	=	surface distance along cone generatrix [m]
$t$	=	time [sec]
$T_{w,adb}$	=	adiabatic wall temperature [K]
$T_w$	=	wall temperature [K]
$T_\infty$	=	freestream temperature [K]
$N$	=	N-factor of linear instabilities
$X$	=	axial coordinate [m]
$Y$	=	wall-normal distance [m]
$\alpha$	=	angle of attack [deg]
$\square$	=	azimuthal wavelength [deg or m, depending on context]
$\phi$	=	azimuthal coordinate with respect to windward meridian [deg]
$\tau$	=	total wall shear stress [Pa]
$\tau_\theta$	=	azimuthal wall shear stress [Pa]

## 1. Flow Configuration and Analysis Codes

The flow configuration of interest corresponds to a circular cone at angle of attack to a uniform, hypersonic free stream. The primary configuration for the Purdue experiments corresponds to a 0.457 meter long (18 inches), nominally sharp nosed cone (modeled with a nose radius of  $10^{-4}$  times the cone length) with a half angle of 7 degrees and an angle of attack equal to 6 degrees. The freestream conditions correspond to a free-stream Mach number of  $M = 6$ , unit Reynolds number  $Re = 10.8 \times 10^6$  per meter, and free-stream temperature  $T_\infty = 52.44$  K. The temperature of the model surface,  $T_w$ , is equal to 300 K.

The unperturbed boundary layer flow over the cone is computed using the VULCAN (Viscous Upwind aLgorithm for Complex flow ANalysis) software [48]. The code solves the unsteady, conservation equations appropriate for laminar or turbulent flow of calorically or thermally perfect gases with a spatially second order accurate cell-centered finite volume scheme. A variety of upwind schemes are available for fine-tuning of numerical dissipation and shock capturing in order to ensure solution accuracy for stability computations. In the present computations, the inviscid fluxes were constructed using the MUSCL  $\kappa=0$  scheme, the van Albada gradient limiter [49] and the Low Dissipation Flux Split Scheme (LDFSS) of Edwards [50]. The cell face gradients required to construct the viscous fluxes were obtained using an auxiliary control volume approach that results in a compact viscous stencil that produces a second order accurate approximation of the full Navier-Stokes viscous fluxes. The solutions were relaxed in pseudo time to steady state using the 3-D ILU(0) scheme [51] with a constant CFL number on the order of 50. Grids of  $345 \times 257 \times 353$  and  $345 \times 129 \times 353$  in the axial, azimuthal, and wall-normal directions, respectively, were used. Exploiting the azimuthal symmetry of the boundary layer about the windward and leeward planes, only one half of the circular cone was modeled in the boundary layer computation. In previous work, similar computations of the mean flow over an elliptic cone configuration were cross-validated against the solutions obtained with the LAURA code [52] for various grid sizes [20]. Thus, no extensive grid convergence analysis was deemed necessary. As an illustration, however, Fig. 1 shows the boundary layer profiles obtained using two different grids. An excellent agreement may be observed between the two sets of profiles within the region of interest. Further details on the mean flow solution and its linear stability characteristics may be found in Ref. [17].

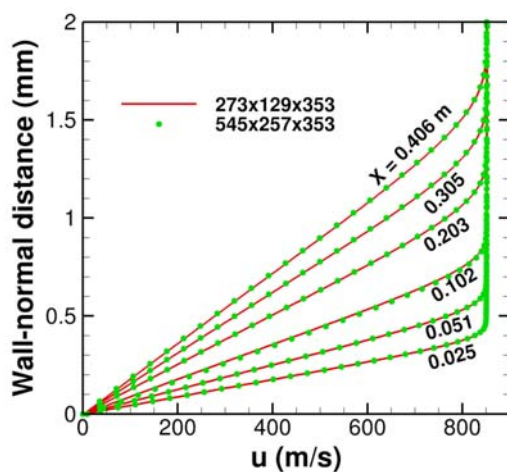


Fig. 1. Effect of grid resolution on mean velocity profiles along  $\phi = 120$  deg.

The evolution of stationary crossflow disturbances in the boundary layer flow is computed by solving the full three-dimensional compressible Navier-Stokes equations in conservation form. To provide a controlled setting for the study of secondary instability, the stationary crossflow vortices are excited via azimuthally periodic forcing with a single azimuthal wavenumber of  $n = 60$ . The forcing is introduced via an array of localized roughness elements centered at  $X = 0.18$  m. The streamwise shape of the roughness elements corresponds to a half-wavelength cosine shape with an axial wavelength of 0.008 m and a peak height

perturbation of 5  $\mu\text{m}$ . The resulting disturbance field is similar to that observed in the experiments by Craig and Saric [25]; however, because the disturbance field in their experiments was excited by uncontrolled background disturbances, no attempt has been made to achieve a precise match with their data. The primary focus of the present study is to characterize the general behavior of secondary instabilities of stationary crossflow vortices in a hypersonic boundary layer, and for that purpose, it is sufficient that the crossflow vortices approximate the strength of nonlinear crossflow vortices as gauged by the rollup of mass-flux contours across the cross-section and the spatial region (axial and azimuthal locations) of vortices with sufficiently large amplitudes.

The working fluid is assumed to be perfect gas (air) and the usual constitutive relations for a Newtonian fluid are used: the viscous stress tensor is linearly related to the rate-of-strain tensor, and the heat flux vector is linearly related to the temperature gradient through the Fourier's law. The coefficient of viscosity is computed from the Sutherlands's law, and the coefficient of thermal conductivity is computed by assuming a constant Prandtl number  $\text{Pr} = 0.71$ . A detailed description of the governing equations and their numerical solution is given by Wu et al. [53]. The inviscid fluxes from the governing equations are computed using a seventh-order weighted essentially non-oscillatory finite-difference WENO introduced by Jiang and Shu [54], the present scheme is optimized by means of limiters [53, 55] to reduce the numerical dissipation. Both an absolute limiter on the WENO smoothness measurement and a relative limiter on the total variation are employed simultaneously during the simulation. The viscous fluxes are discretized using a fourth-order central difference scheme and time integration is performed using a third-order low-storage Runge-Kutta scheme [56]. The numerical code has been previously applied to simulation of turbulence in hypersonic boundary layers [57] as well as laminar-turbulent transition due to crossflow instability in swept wing boundary layers [58, 59]. The lessons learned from these simulations were applied to develop the computational grid for stationary crossflow evolution in the present work.

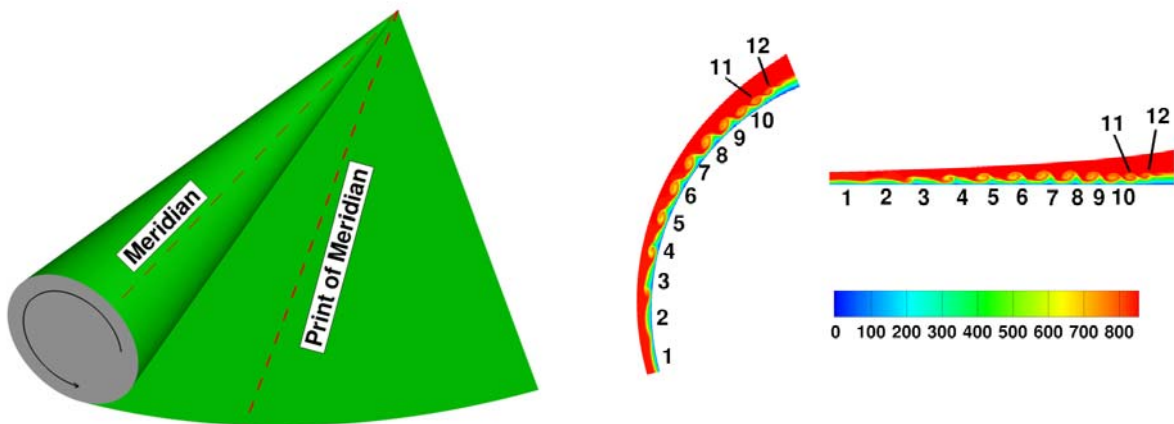
The primary instability computation is performed on a grid consisting of  $600 \times 1200 \times 160$  points in the axial, azimuthal, and radial directions, respectively. Without any loss of generality, the stationary crossflow disturbances are assumed to be symmetric about the windward and leeward planes, so that only one half of the circular cone was included in the computational domain. The grid points are spaced uniformly in the azimuthal direction.

The secondary instability of the finite amplitude stationary crossflow vortices computed using DNS is investigated using two different methods. The first method corresponds to a quasi-parallel analysis of spatial instability as described by Li and Choudhari [60, 61], whereas the second technique accounts for the leading-order non-parallel effects using the framework of parabolized stability equations as described by Paredes et al. [62, 63]. The results presented in this paper are exclusively based on the quasi-parallel method. Predictions based on the PSE are deferred to a follow-on paper.

In principle, the quasi-parallel stability formulation can be extended to include the effects of surface curvature. In the present paper, however, those effects are assumed to be a higher order correction that is comparable to the effects of mean-flow non-parallelism. Because the wavelength of the crossflow instability is comparable to the thickness of the boundary layer, the above assumption is consistent with the high Reynolds number asymptotic limit underlying the boundary layer approximation. Instability analysis in the absence of surface curvature amounts to unrolling the cone surface onto a plane. If one were to coat the cone with paint and roll it on a flat surface, the resulting printed area in the shape of a fan would represent the cone-to-plane mapping (Fig. 2(a)), with a one-to-one correspondence between the points on the cone and those on the unrolled flat surface. The left half of Fig. 2(b) shows the axial velocity contours in a subset of a typical cross-section of the cone in the presence of stationary crossflow vortices, and its map onto a domain resting on the flat, unrolled surface is shown in the right half of Fig. 2(b). For later reference, the vortices most easily discernible from their surface signature are numbered 1 through 12 in the figure. The azimuthal extent of each vortex at a given axial station is determined by the distance between the two points on either side of the vortex where the wall shear in the meridian direction is a local maximum. The vortex is then made

spanwise periodic via detrending and Fourier low-pass filtering to facilitate local secondary instability computations. In the computational volume with the flattened (i.e., unrolled) base, the  $X$ -direction is taken as the meridian direction, i.e., the direction along any line joining a point on the flat surface and the virtual vertex of the fan. The local spanwise direction at a point is along the azimuthal coordinate at a fixed axial location over the surface of the cone. The mean flow resulting from these modifications is now amenable to both temporal and spatial stability analyses using the procedure described in Refs. [60, 61] in the context of crossflow modes in swept-wing boundary layers.

Because the mean flow modified by the presence of crossflow vortices involves comparable length scales in both azimuthal and radial directions (see Fig. 2(b)), the basic state for secondary instability is inhomogeneous in two spatial directions. Hence, predicting the amplification characteristics of secondary instability modes leads to a planar (i.e., 2D), partial differential equation based eigenvalue problem, rather than an ordinary differential equation based eigenvalue problem that is obtained in a classical analysis of primary instabilities in a shear flow that has strong gradients only along the wall-normal coordinate. The selection of grid and other aspects of the numerical solution were based on extensive experience with a similar class of flows (see, for instance, Refs. [64, 65]) and checks were made to ensure that the impact of variations with respect to those choices was negligible. Typically, the 2D eigenvalue problem corresponding to linear secondary instability was solved using 121 points along the wall-normal direction and between 33 to 65 grid points along the azimuthal direction.



(a) Surface unrolling on a plane. The two dashed lines represent a meridian line on the cone and its imaginary print on the plane, respectively.

(b) Correspondence between original and unrolled domains at a given  $X$  along with streamwise velocity contours.

**Fig. 2. Schematic of quasi-parallel secondary instability analysis.**

## 2. Results

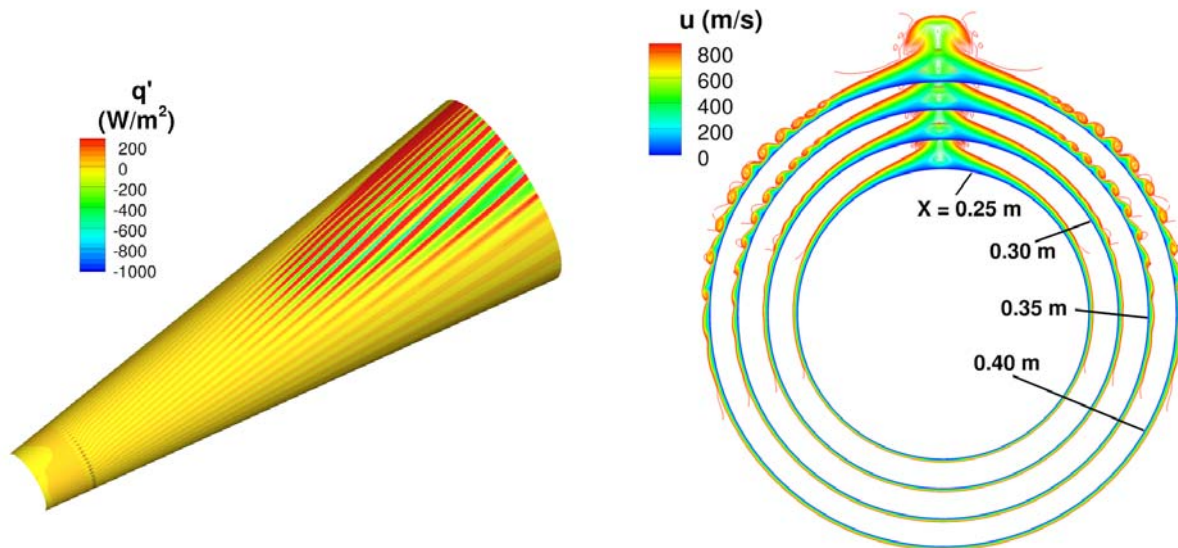
Computational results pertaining to both primary and secondary instabilities of the boundary layer flow over the cone are presented in this section. The evolution of stationary crossflow vortices excited by an azimuthally periodic array of localized roughness elements is described first in Section 2.1. The instability characteristics of selected vortices are investigated in Section 2.2.

### 2.1 Evolution of Stationary Crossflow Vortices

The stationary crossflow vortices leave an imprint on the cone surface in the form of longitudinal streaks in surface heat transfer as shown in Fig. 3(a). Immediately downstream of the forcing location, the vortex wavelength is approximately uniform along the azimuthal direction and corresponds to the forcing wavenumber of  $n = 60$ . The latter wavenumber was chosen to approximate the azimuthal wavelength of the crossflow modes found in the experiments of Craig and Saric [25]. Farther downstream from the forcing

location, the streaks generated by the roughness element pattern progressively move towards the leeward ray and the streak spacing changes as a result of non-parallel flow effects. As discussed in Ref. [66], there is a pronounced difference between the larger vortex wavelength near the sideline ray and the smaller wavelength on the leeward side.

Axial velocity contours at selected streamwise stations are shown in Fig. 3(b). For the forcing location selected in this study ( $X=0.18$  m), the dominant crossflow vortices near the end of the computational domain lie between the sideline ray ( $\phi = 90$  deg) and the leeward ray ( $\phi = 180$  deg), analogous to that in the previously mentioned experimental investigations [21–25]. The velocity contours at  $X = 0.35$  m and  $0.40$  m reveal the strongly nonlinear structure of crossflow vortices that qualitatively resembles the hot wire measurements of Craig and Saric [25].

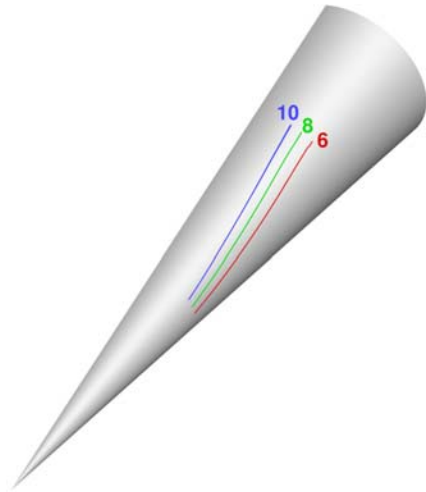


(a) Contours of wall heat flux perturbation.

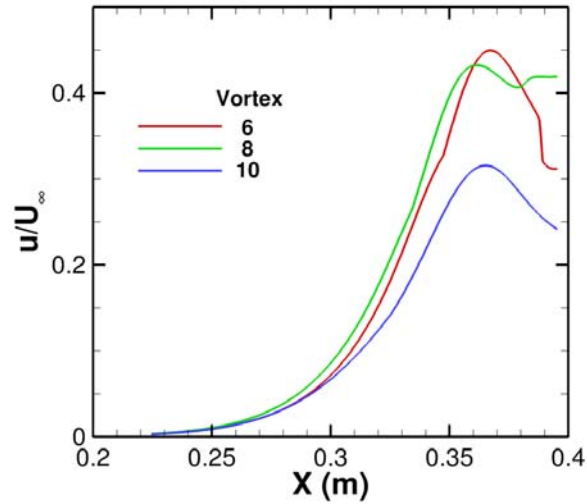
(b) Axial velocity contours at selected locations.

**Fig. 3. Evolution of stationary crossflow vortices excited by azimuthally periodic array of localized roughness elements.**

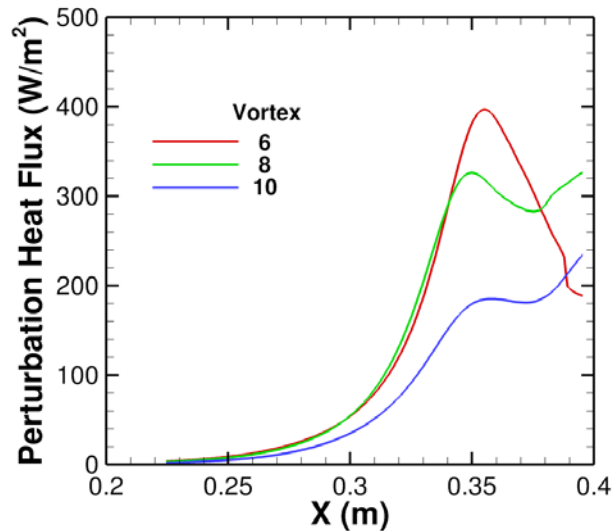
Trajectories of selected vortices and the corresponding evolution of vortex amplitude along the cone length are shown in Figs. 4(a) and 4(b)-(c), respectively. Vortices 6 through 10 correspond to the highest velocity perturbations among those shown in Fig. 4(a). The amplitude plotted in Fig. 4(b) corresponds to the peak axial velocity perturbation over the cross section of the vortex, whereas the vortex amplitude shown in Fig. 4(c) corresponds to the peak heat flux perturbation. Over most of the region shown in Fig. 4(b), vortex 8 has the highest velocity perturbation of all vortices. At  $X = 0.25$  m, all three vortices have relatively small amplitudes, less than approximately two percent of the freestream velocity. By  $X = 0.30$  m, the vortex amplitudes have increased to somewhere between five to eight percent, whereas by  $X = 0.35$  m, all three vortices have amplitudes in excess of 25 percent. The peak amplitude achieved by vortex 6 near  $X = 0.35$  m is almost 45 percent of the freestream velocity. The corresponding peak heat flux amplitudes in Fig. 4(c) are comparable to those measured in the experiments at Purdue University [21, 23, 67].



(a) Selected vortex trajectories.



(b) Vortex amplitudes measured by peak axial velocity perturbation.

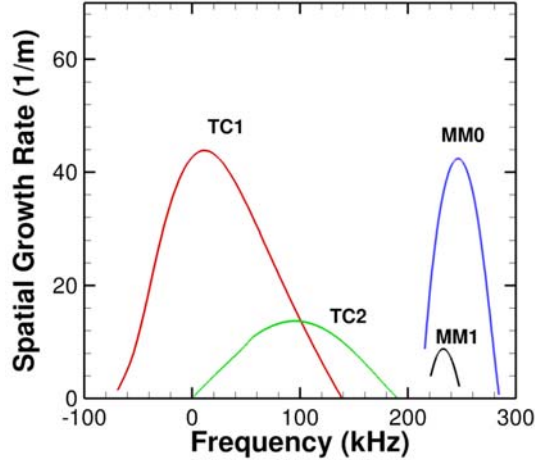


(c) Vortex amplitudes in terms of surface heat transfer.

**Fig. 4. Stationary crossflow vortices selected for secondary instability analysis.**

## 2.2 Secondary Instability Characteristics

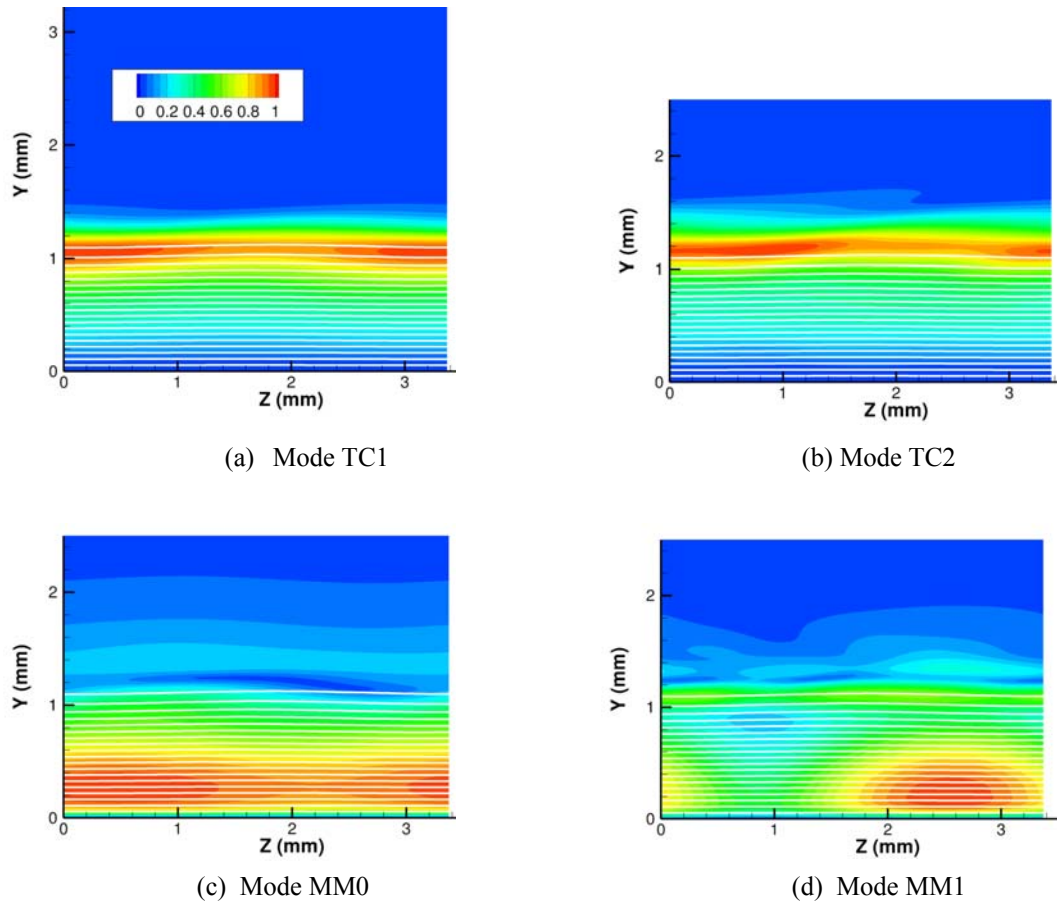
The procedure for instability analysis outlined in Section 1 was applied to the basic state described in Section 2.1. A representative spectrum of unstable modes is shown in Fig. 5, wherein the spatial growth rate of dominant instabilities has been plotted as a function of frequency for vortex 10 at  $X=0.25$  m. At  $X=0.25$  m, the amplitude of the primary crossflow vortex is relatively weak so that the predicted secondary instabilities are approximately equivalent to the primary instabilities of the unperturbed cone boundary layer with the additional constraint that the azimuthal wavenumber of the secondary mode be consistent with the local wavelength of the stationary vortex.



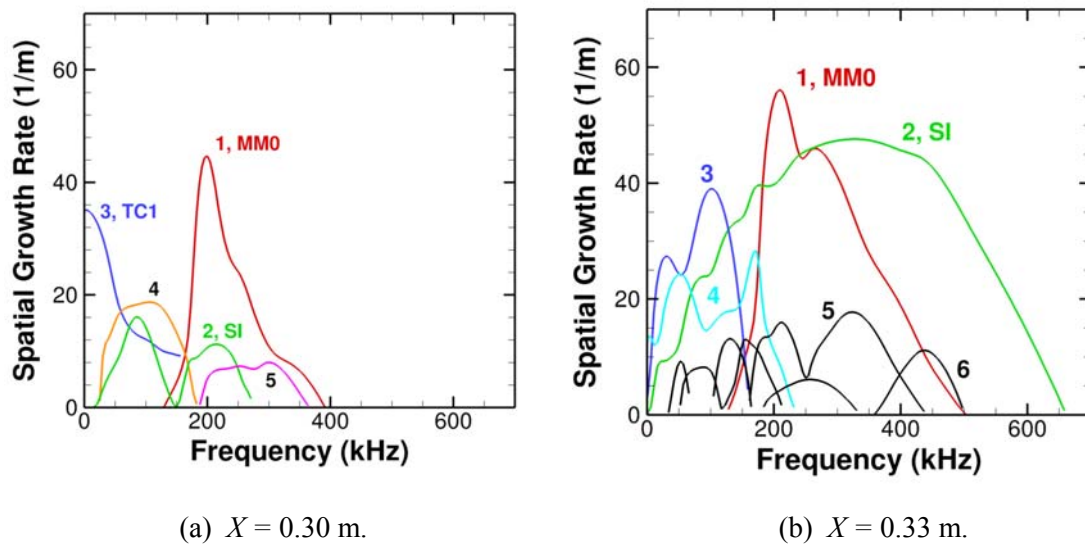
**Fig. 5. Instability characteristics as a function of frequency at an upstream station (vortex 10,  $X = 0.25$  m).**

Figure 5 shows that the unstable secondary disturbances are concentrated in two separate frequency ranges. The low-frequency lobes (with peak frequencies below approximately 100 kHz) correspond to traveling crossflow instability modulated by the weak stationary crossflow vortex. Accordingly, they are labeled as TC1 and TC2, respectively, where the numerical suffix identifies the index of the azimuthal harmonic corresponding to the stationary mode. Thus, the mode TC1 corresponds to secondary modes with an azimuthal wavenumber equal to the local fundamental wavenumber of the stationary vortex, whereas mode TC2 corresponds to a secondary mode with an azimuthal wavenumber equal to twice the fundamental wavenumber. In a similar manner, the two high-frequency lobes correspond to second mode (i.e., Mack mode) waves of the unperturbed boundary layer over the cone, and hence, have been labeled MM0 and MM1, respectively. The mode MM0 corresponds to axisymmetric Mack mode whereas mode MM1 corresponds to an oblique Mack mode with an azimuthal wavenumber equal to that of the stationary crossflow vortex. Because the growth rate of second mode disturbances decreases rapidly with the wave angle, only the fundamental harmonic is unstable in this case. Representative mode shapes for the above families of disturbances are shown in Figs. 6(a) through 6(d). Peak velocity fluctuations associated with the Mack modes are relatively close to the surface, whereas those associated with the traveling crossflow modes are concentrated further away inside the boundary layer. In the remaining part of this paper, we focus mainly on the high-frequency disturbances since they appear to be linked more closely with the observed onset of laminar breakdown in the Purdue experiments [21, 22].

As the amplitude of the stationary crossflow vortex increases in the downstream direction, the modal topology gets progressively modified and it becomes difficult to attribute a clear mode type to each family of unstable secondary disturbances, especially to the low-frequency modes, unlike that in Fig. 5. Hence, the unstable modes at downstream locations are denoted simply using a numerical index, ordered approximately in the order of decreasing peak growth rate at the location of interest. A total of six dominant modes were selected for the plot in Fig. 7(a) at  $X = 0.30$  m. Additional modes with relatively low peak growth rates have been omitted from the plot to avoid visual clutter. Representative mode shapes for the modes shown in Fig. 7(a) are plotted in Fig. 8.



**Fig. 6. Representative mode shapes for secondary disturbances from Fig. 5. Coordinate  $Z$  denotes the azimuthal distance along the surface whereas  $Y$  denotes the wall-normal distance from the cone surface.**



**Fig. 7. Growth rate spectra for vortex 10 at selected downstream locations**

Results at intermediate locations (not shown herein) suggested that the maximum growth rate of the oblique Mack mode (mode MM1 in Fig. 5) decreases with increasing  $X$  (and correspondingly, with a higher crossflow

vortex amplitude). Therefore, at locations sufficiently far downstream, the only dominant high-frequency mode related to the Mack mode instabilities at upstream stations corresponds to a modified version of mode MM0 (corresponding to mode 1 in Fig. 7(a)). A comparison of Figs. 6(c) and 8(b) indicates how the original, azimuthally nearly uniform mode shape has been distorted by the stationary crossflow vortex. On the other hand, a new high frequency mode (mode 2 in Fig. 7(a)) that was not present at the upstream stations with low vortex amplitudes has emerged at  $X = 0.30$  m. The peak growth rate of this new mode is small at this location, but becomes nearly the same as the growth rate of mode MM0 farther downstream. The mode shape of this new mode bears a remarkable resemblance to the secondary instability mode driven by the spanwise shear of the crossflow vortex in swept-airfoil boundary layers [65, 68]. Thus, mode 2 apparently represents a genuine secondary instability of the finite amplitude crossflow vortex over the cone, and hence, is denoted alternatively by the nomenclature of SI. The peak-growth frequency of this mode is even higher than that of the mode MM0 and the range of unstable frequencies  $X = 0.33$  m is very broad, extending from almost 0 kHz to over 600 kHz. The large frequency bandwidth of this mode appears consistent with its interpretation as an instability of the relatively thin, inclined shear layer associated with the overturning contours of axial velocity associated with a strong crossflow vortex (Fig. 3(b)).

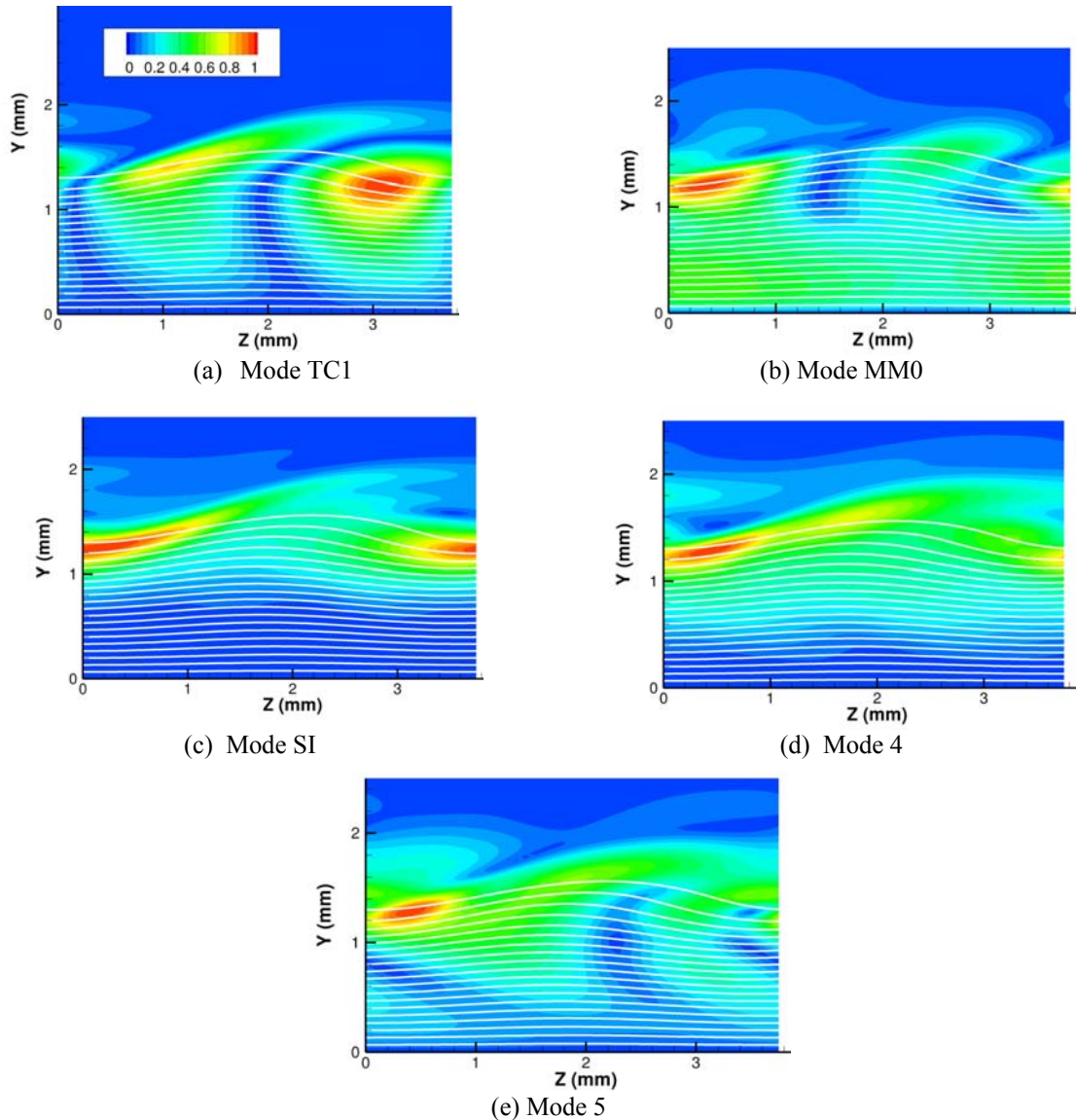


**Fig. 8. Representative  $|u'|$  mode shapes for secondary instabilities of vortex 10 at  $X = 0.30$  m.**

Since the unsteady disturbance spectra in Refs. [20-23] were measured via surface pressure transducers, the disturbance mode shapes for pressure fluctuation magnitudes for MM0 and SI modes at  $X=0.30$  m are shown in Figs. 9(a) and 9(b), respectively. Analogous results for  $X=0.33$  m are plotted in Figs. 10(a) and 10(b). The figures show that the peak pressure fluctuations for the MM0 mode occur near the surface. As expected, azimuthal variations in surface pressure amplitudes becomes more pronounced as the vortex amplitude increases from  $X=0.30$  m to  $X=0.33$  m. The highest pressure fluctuations associated with the SI modes are concentrated away from the surface, approximately at the same location as the peak velocity fluctuations. The peak surface pressure fluctuations at the surface are approximately two times weaker than those at the interior peak.

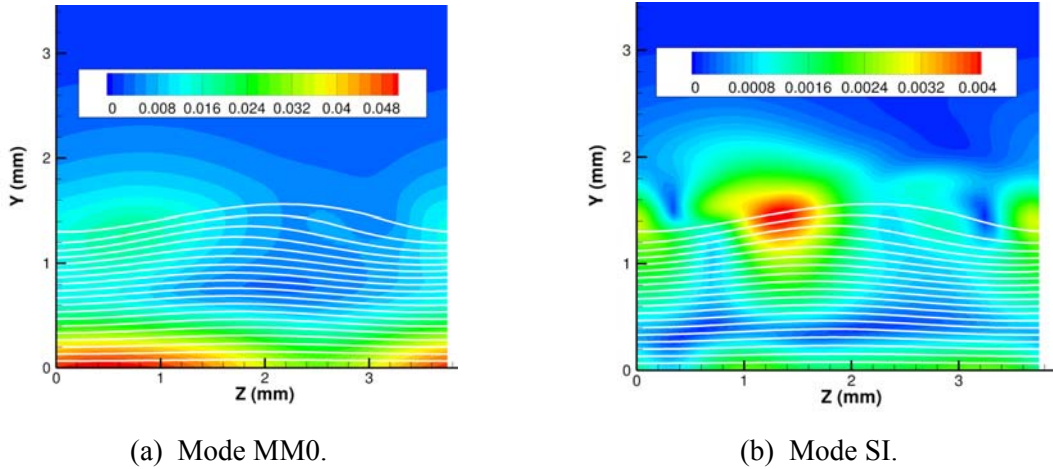


**Fig. 9.  $|p'|$  mode shapes for secondary disturbance types MM0 and SI ( $X = 0.3$  m).**

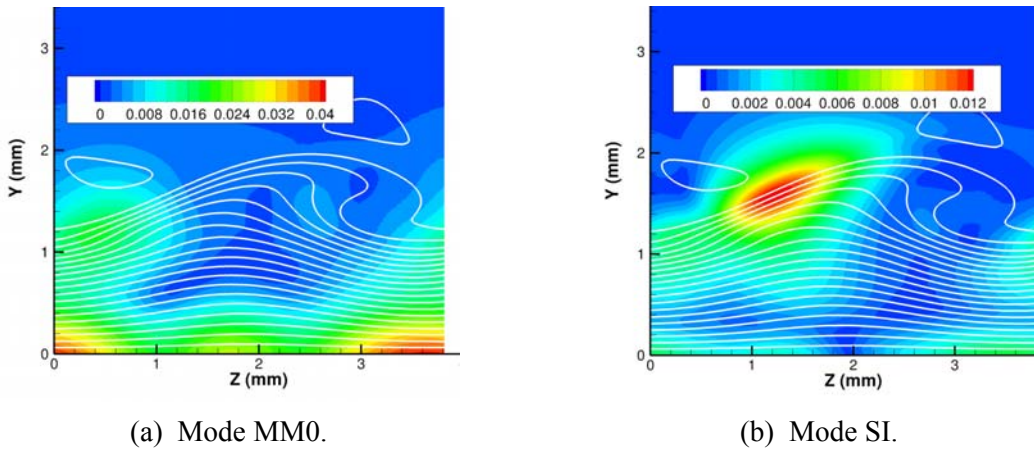


**Fig. 10.  $|p'|$  mode shapes for secondary disturbance types MM0 and SI ( $X = 0.33$  m).**

The cumulative growth characteristics for the most unstable MM0 and SI modes are considered next. Figure 11(a) shows the variation of the logarithmic amplification ratio, i.e., N-factor, along the cone length for selected frequencies of vortex 10 instabilities. Corresponding results for vortex 6 are shown in Fig. 11(b). Each red curve denotes a fixed frequency MM0 mode, whereas the green curves denote the SI modes. For vortex 10, the most amplified MM0 mode has a frequency of approximately 235 kHz, whereas the peak frequency of the SI mode is significantly higher, being equal to 320 kHz. The N-factor curves in Fig. 11(a) imply that the MM0 modes of vortex 10 begin to amplify when the stationary crossflow modes are still very weak. Consistent with typical second (i.e., Mack) mode behavior, the growth rates begin to decrease within a relatively short distance after their onset and then increase again as the amplitude of the stationary crossflow

vortex increases. For some disturbance frequencies, the latter increase is preceded by a modest decay in the amplitude of the MM0 mode. In contrast to the MM0 mode, the onset of SI modes occurs only after the amplitude of the crossflow vortex has become sufficiently large. In the range of approximately  $X=0.35$  m to  $X=0.40$  m (where vortex 10 has its largest amplitudes), the peak growth rates of the SI mode are larger than the peak growth rates of the MM0 mode as indicated by the relative slopes of the corresponding N-factor curves. However, the peak N-factor of the SI modes at the end of the 0.40 meter length of the Purdue cone remains slightly smaller than the peak N-factor associated with the modified Mack modes. The N-factor differential between the two modes is approximately equal to one. The reader may also recall from Figs. 9 and 10 that the mode MM0 has a stronger signature at the surface than the SI mode.

Compared to vortex 10, SI growth for vortex 6 begins farther downstream and the peak growth rates remain smaller. Consequently, the overall growth of the high-frequency disturbances over vortex 6 is entirely dominated by the MM0 mode. The reasons behind the lower N-factors of SI modes of vortex 6 are not entirely clear. They might be related to the larger spanwise wavelength of the crossflow vortices farther away from the leeward plane (since a larger wavelength would imply weaker azimuthal gradients of the basic state to facilitate energy transfer to the secondary instabilities) or the observation that the velocity amplitude of vortex 6 decreases rapidly after achieving its peak near  $X=0.37$  m (Fig. 4(b)). The maximum SI-mode N-factor for vortex 8 is in between that for vortices 6 and 10.

The envelope of the N-factor curves for the MM0 mode appears to level off between approximately  $X=0.25$  and  $X=0.3$  m, and as the primary stationary vortex becomes even stronger downstream of this region, the N-factor envelope begins to rise again. In the absence of the stationary crossflow vortex, the maximum N-factors of second mode disturbances would remain below  $N=2$ . The substantial increase in N-factors of the MM0 modes in the region of high crossflow amplitudes illustrates the dramatic effect of the modulation of the MM0 mode by the large amplitude crossflow vortex.

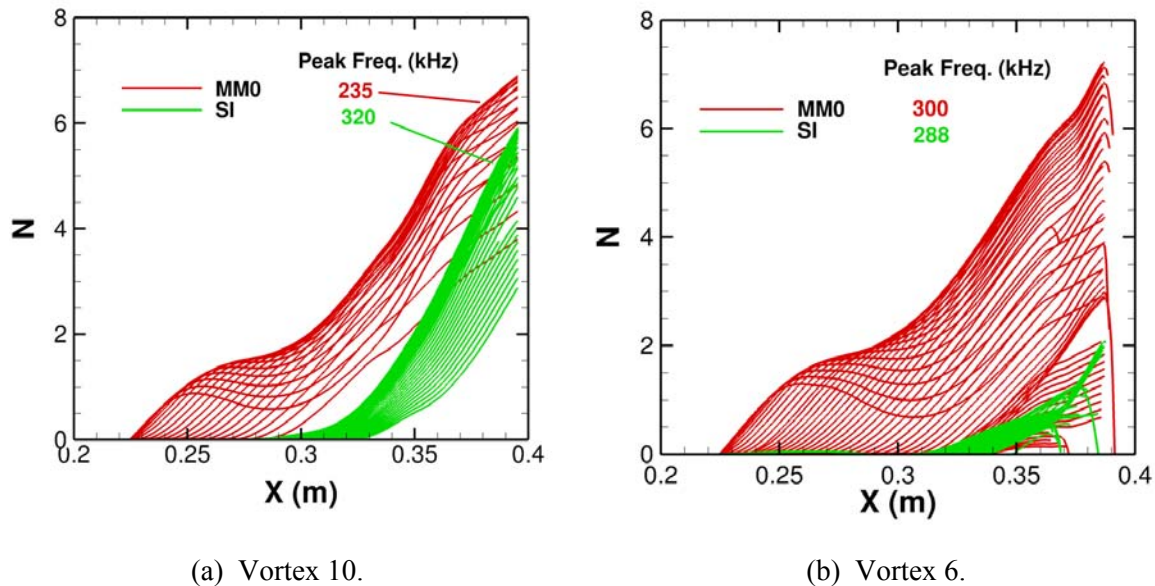
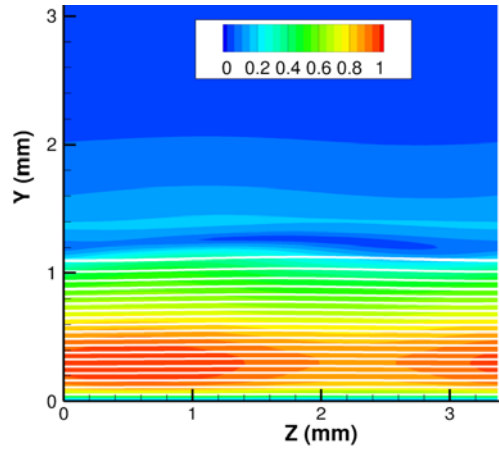
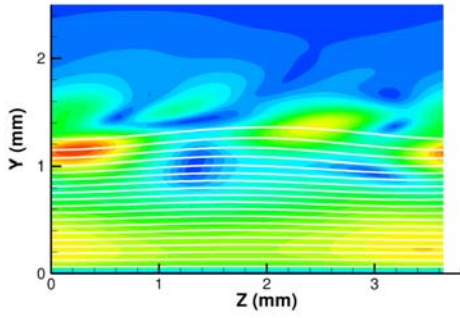


**Fig. 11. N-factor evolution along selected vortices.**

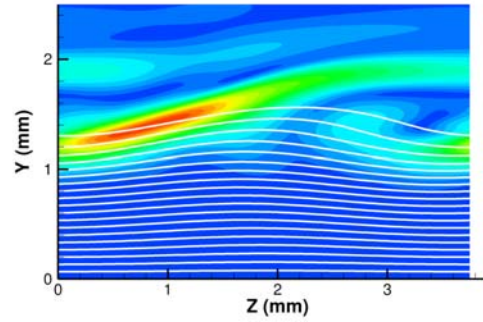
Mode shape evolution for the MM0 and SI modes of vortex 10 with the highest amplification ratios is shown in Fig. 12. The evolution of velocity disturbances associated with the MM0 mode indicates how the peak fluctuations rise above the surface with increasing downstream distance. On the other hand, the mode shape of the SI mode remains very similar throughout the evolution of this mode, being concentrated along the inclined shear layer as mentioned previously.



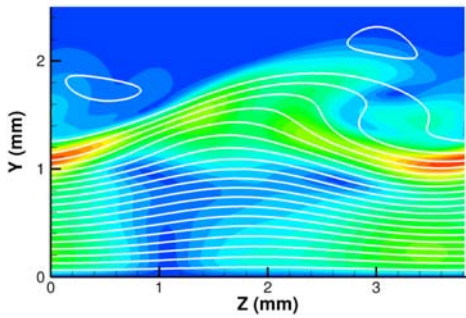
(a) Mode MM0,  $X = 0.25$  m



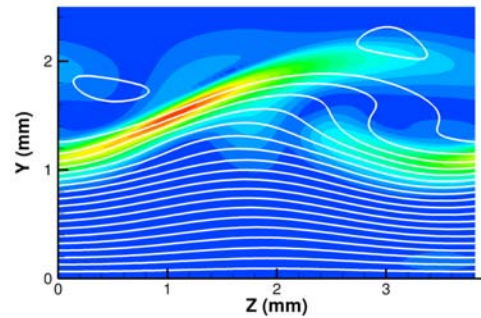
(b) Mode MM0,  $X = 0.28$  m



(c) Mode SI,  $X = 0.30$  m



(d) Mode MM0,  $X = 0.325$  m



(e) Mode SI,  $X = 0.325$  m

**Fig. 12. Streamwise evolution of  $|u'|$  mode shapes for dominant instabilities of vortex 10 (continued).**

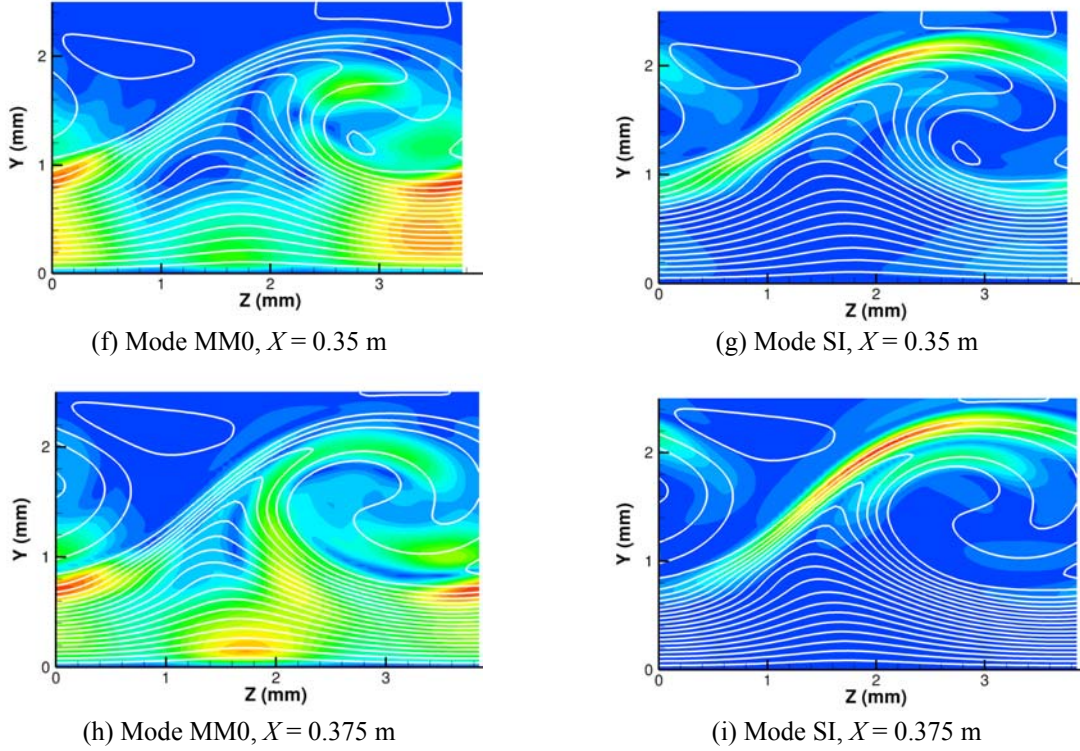


**Fig. 12. Concluded.**

A comparison of the results plotted in Figs. 11(a) and 11(b) shows that the peak frequency of MM0 mode decreases from vortex 6 to vortex 10 because of the increase in boundary layer thickness from windward to leeward planes. On the other hand, the frequency of the SI Mode is strongly influenced by the characteristics of the inclined shear layer, which are determined by the wavelength and amplitude of the stationary crossflow vortex. Thus, one finds, in fact, that the peak disturbance frequency of the SI mode as predicted via the quasi-parallel stability theory employed herein increases from vortex 6 to vortex 10.

Both experiments [69] and computations [70–75] of crossflow breakdown in subsonic swept-wing boundary layers have shown that the high-frequency secondary instabilities can rapidly amplify by orders of magnitude to initiate the onset of transition. Even though the SI modes have large growth rates in the present, hypersonic case, the modified Mack modes also play an important role and may in fact correspond to higher amplification ratios than the SI modes. Thus, future computations of nonlinear interactions involving the broader set of high-frequency modes would be of great interest.

Figure 13 shows the azimuthal variation in growth rate spectra for modes MM0 at  $X = 0.33$  m. In particular, growth rate spectra for vortices 6, 8, and 10 are shown as functions of the disturbance frequency. The peak frequency of the MM0 modes is the highest for vortex 6 and lowest for vortex 10. The variation in peak frequency is qualitatively consistent with the accompanying increase in underlying boundary layer thickness. Unlike the MM0 modes, the peak frequency of the SI modes does not show any pronounced variation from vortex 6 to vortex 8. On the other hand, unlike the MM0 modes, the peak growth rate of the SI Modes increases substantially from vortex 6 to vortex 10, in spite of the fact that the peak velocity amplitude of vortex 10 at  $X = 0.33$  m is lower than the amplitudes of the other two vortices. The variation in growth rate may be related to the smaller azimuthal wavelength of vortex 10, which implies potentially stronger azimuthal gradients in the basic state that drive this particular mode of secondary instability.

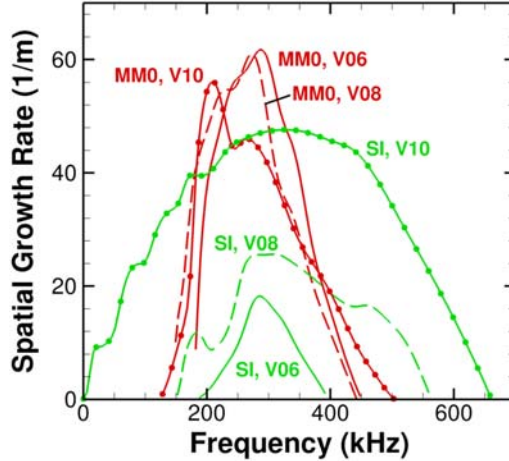


**Fig. 13.** Variation in growth rate spectra along azimuthal direction ( $X = 0.33$  m). The curves denoted as V06, V08, and V10 indicate the growth rate variations for vortices 6, 8, and 10, respectively.

### 3. Summary and Concluding Remarks

Quiet tunnel experiments at Purdue University [21] have detected high-frequency disturbances in the vicinity of an apparent breakdown of large amplitude stationary crossflow vortices during their experiments on a yawed circular cone in the Mach 6 BAMQT facility at Purdue University. The observed dependence of these high-frequency disturbances on a threshold stationary wave amplitude and their localized azimuthal signature led these investigators to suggest that these disturbances were caused by the secondary instability of the stationary crossflow modes. In contrast, Munoz et al. [20] attributed the high-frequency measurements in a conventional facility to second mode waves. The instability analysis in this paper shows that the high-frequency disturbances may be attributed to both second mode waves modified by finite amplitude crossflow vortices and a genuine secondary instability of the stationary vortices.

At sufficiently high stationary crossflow amplitudes, the original second mode (i.e., Mack mode) disturbances are further destabilized, resulting in peak growth rates that are significantly larger than those of second modes in the absence of any crossflow vortices. Large amplitude crossflow vortices also lead to a genuinely new instability mode (mode SI) that corresponds to secondary instability of the azimuthally modulated boundary layer. Unlike the second mode disturbances, the SI mode is unstable over a broad range of frequencies and its mode shapes are similar to the secondary instabilities driven by spanwise basic-state shear in subsonic swept wing boundary layers. The frequencies of the most amplified modified Mack modes and the SI mode are in the range of 200 kHz to 300 kHz, with noticeable variation depending on the location of interest and the amplitude of the crossflow vortex. The above frequency range is approximately consistent with the frequencies measured in the experiments at Purdue University [21–23] and the Technical University of Braunschweig [20]. However, additional computations to assess the role of the modeling approximations employed in the present work are deemed highly desirable. In particular, the effect of non-parallel evolution of the basic state for secondary instability must be examined. Given the richness of the unstable secondary modes within a relatively small range of phase speeds, it is possible that the non-parallel effects would lead to significant changes in the modal topology and, hence, in the evolution of the N-factor envelopes. Computations of this type are currently in progress and the results thereof will be reported in a separate paper.

Finally, the spatial structure of the computed SI mode is similar to the measured mode shape of the so-called high-frequency modes in the quiet tunnel experiments [25] at Texas A&M University. However, the present SI mode has substantially higher frequencies than the 80-120 kHz range measured in those experiments. Thus, the origin of the latter modes remains to be determined.

The presence of multiple SI modes in the Mach 6 configuration of interest is analogous to the secondary instability of crossflow vortices over subsonic and supersonic airfoils. Computations for the subsonic boundary layers have shown that nonlinear effects tend to reduce the growth of the secondary instability modes. However, if the amplitudes become sufficiently large, then a rapid breakdown to turbulence can ensue. Whether or not a similar scenario prevails at hypersonic Mach numbers, where the modified Mack modes also play an important role, remains to be seen. The follow-on work will focus on the breakdown mechanisms and the strongly nonlinear phase of transition to turbulence at hypersonic speeds.

## References

1. Mack, L.M., Boundary-Layer Linear Stability Theory, in “Special Course on Stability and Transition of Laminar Flow,” AGARD Report No. 709, pp. 3–1 to 3–81, 1984.
2. Li, F., Choudhari, M. M., Chang, C.-L., Wu, M. and Greene, P. T. “Development and Breakdown of Görtler Vortices in High Speed Boundary Layers,” AIAA Paper 2010-705, 2010.
3. Saric, W.S., Reed, H.L., and White, E.B., “Stability and Transition of Three-Dimensional Boundary Layers,” *Ann. Rev. Fluid Mech.*, Vol. 35, pp. 413–40, 2003.
4. Dougherty, N. S. and Fisher, D. F., “Boundary Layer Transition on a 10-degree Cone: Wind Tunnel/Flight Data Correlation,” AIAA Paper 80-0154, 1980.
5. King, R. A., “Three-Dimensional Boundary-Layer Transition on a Cone at Mach 3.5,” *Experiments in Fluids*, Vol. 13, No. 5, pp. 305–314, 1992.
6. Malik, M. R. and Balakumar, P., “Instability and Transition in Three-Dimensional Supersonic Boundary Layers,” AIAA Paper 1992-5049, 1992.
7. Hanifi, A. and Dahlkild, A.A., “Some Stability Characteristics of the Boundary Layer on a Yawed Cone,” AIAA Paper 1993-3048, 1993.
8. Sugiura, H., Tokugawa, N., Nishizawa, A., Ueda, Y., Ishikawa, H., and Yoshida, K., “Boundary-Layer Transition on Axisymmetric Bodies with Angles of Attack in Supersonic Flow,” Proceedings of 2003 Annual Meeting, Japan Society of Fluid Mechanics, pp. 352-353, 2003 (in Japanese).
9. Balakumar, P., “Stability of Supersonic Boundary Layers on a Cone at an Angle of Attack,” AIAA Paper 2009-3555, 2009.
10. Tokugawa, N., Choudhari, M., Ishikawa, H., Ueda, Y., Fujii, K., Atobe, T., Li, F., Chang, C.-L. and White, J., “Transition Along Leeward Ray of Axisymmetric Bodies at Incidence in Supersonic Flow,” *AIAA Journal*, Vol. 53, No. 12, 2015, pp. 3737–3751. doi: 10.2514/1.J054070
11. Choudhari, M., Tokugawa, N., Li, F., Chang, C.-L., White, J., Ishikawa, H., Ueda, Y. Atobe, T. and Fujii, K., “Computational Investigation of Supersonic Boundary Layer Transition over Canonical Fuselage Nose Configurations,” Proc. of 7<sup>th</sup> Intl. Conference on Computational Fluid Dynamics, Island of Hawaii, June 2012 ([http://www.iccfd.org/iccfd7/assets/pdf/papers/ICCFD7-2306\\_paper.pdf](http://www.iccfd.org/iccfd7/assets/pdf/papers/ICCFD7-2306_paper.pdf)).
12. Schuele, C. Y., Corke, T. C., and Matlis, E., “Control of Stationary Crossflow Modes in a Mach 3.5 Boundary Layer Using Patterned Passive and Active Roughness,” *Journal of Fluid Mechanics*, Vol. 718, 2013, pp. 5–38.
13. Stetson, K.F., Thompson, E.R., Donaldson, J.C., and Siler, L.G., “Laminar Boundary Layer Stability Experiments on a Cone at Mach 8 – Part 3: Sharp Cone at Angle of Attack,” AIAA Paper 85-0492, 1985.
14. Schneider, S.P., “Hypersonic Laminar-Turbulent Transition on Circular Cones and Scramjet Forebodies,” *Prog. in Aerospace Sciences*, Vol. 40, pp. 1–5, 2004.

15. Swanson, E., "Boundary-Layer Transition on Cones at Angle of Attack in a Mach 6 Quiet Tunnel," Ph.D. Dissertation, School of Aeronautics and Astronautics, Purdue University, 2008.
16. Swanson, E. and Schneider, S.P., "Boundary-Layer Transition on Cones at Angle of Attack in a Mach-6 Quiet Tunnel," AIAA Paper 2010-1062, 2010.
17. Li, F., Choudhari, M., Chang, C.-L. and White, J., "Analysis of Instabilities in Non-Axisymmetric Hypersonic Boundary Layers over Cones," AIAA Paper 2010-4643, 2010.
18. Balakumar, P. and Owens, L., "Stability of Hypersonic Boundary Layers on a Cone at Angle of Attack," AIAA Paper 2010-4718, 2010.
19. Li, F., Choudhari M., Chang, C.-L., White, J. A., Kimmel, R., Adamczak, D., Borg, M., Stanfield, S., and Smith, M., "Stability Analysis for HIFiRE Experiments," 42nd AIAA Fluid Dynamics Conference and Exhibit, New Orleans, LA, June 25-28, 2012.
20. Munoz, F., Heitmann, D., and Radespiel, R., "Instability Modes in Boundary Layers of an Inclined Cone at Mach 6," *J. Spacecraft and Rockets*, Vol. 51, No. 2, March 2014, pp. 442–454.
21. Ward, C. A. C., Henderson, R. O., and Schneider, S. P., "Possible Secondary Instability of Stationary Crossflow Vortices on an Inclined Cone at Mach 6," AIAA Paper 2015-2773, 2015.
22. McKiernan, G. R., Chynoweth, G. R., Edelman, J. B., McKenzie, J. A., Sweeney, C. J., "Instability and Transition Experiments in the Boeing/AFOSR Mach 6 Quiet Tunnel," AIAA Paper 2015-2317, 2015.
23. Edelman J. and Schneider, S. P. "New Measurements of the Secondary Instability of Stationary Crossflow Waves in the Mach 6 Quiet Tunnel," NATO-STO AVT-240 & RTG-082 Meeting on Hypersonic Boundary Layer Transition, Prague, Czech Republic, Oct. 15-16, 2015.
24. Craig S.A, Saric W, "Crossflow Instability on a Yawed Cone at Mach 6," 8th IUTAM Symposium on Laminar-Turbulent Transition, Procedia IUTAM, Vol. 14, Medeiros. M. A. F. and Meneghini, J. R. (eds.), 2015, pp. 15–25.
25. Craig, S. A. and Saric, W. S., "Experimental Study of Crossflow Instability on a Mach 6 Yawed Cone," AIAA Paper 2015-2774, 2015.
26. Oliviero, N. B., Kocian, T. S., Moyes, A. J., and Reed, H. L., "EPIC: NPSE Analysis of Hypersonic Crossflow Instability on Yawed Straight Circular Cone," AIAA Paper 2015-2772, 2015.
27. Stanfield, S., Kimmel, R. A., Adamczak, D., and Juliano, T., "Boundary-Layer Transition Experiment During Reentry of HIFiRE-1," *J. Spacecraft and Rockets*, Vol. 52, 2015, pp. 637-649.
28. Juliano, T., Kimmel, R. A., Willems, S., Guelhan, A., and Wagnild, R., "HIFiRE-1 Boundary-Layer Transition: Ground Test Results and Stability Analysis," AIAA Paper 2015-1736, 2015.
29. Li, F., Choudhari, M., and Paredes, P., "Nonlinear Evolution and Secondary Instability of Crossflow Disturbances in Hypersonic Boundary Layer over a Cone," NATO-STO AVT-240 & RTG-082 Meeting on Hypersonic Boundary Layer Transition, Prague, Czech Republic, Oct. 15-16, 2015.

30. Kimmel, R., "Laminar-Turbulent Transition in a Mach 8 Elliptic Cone Flow," *AIAA J.*, Vol. 37, No. 9, pp. 1080–1087, 1999.
31. Poggie, J. and Kimmel, R., "Traveling Instability Waves in a Mach 8 Flow over an Elliptic Cone," *AIAA J.*, Vol. 38, No. 2, pp. 251–258, 2000.
32. Kimmel, R. L., and Poggie, J., "Transition on an Elliptic Cone at Mach 8," American Society of Mechanical Engineers ASME FEDSM97-3111, June 1997.
33. Kimmel, R. L. and Poggie, J., "Three-Dimensional Hypersonic Boundary Layer Stability and Transition," Air Force Research Laboratory Technical Report, WL-TR-97-3111, Wright-Patterson Air Force Base, Ohio, December 1997.
34. Kimmel, R. L., Poggie, J. and Schwoerke, S. N., "Laminar-Turbulent Transition in a Mach 8 Elliptic Cone Flow," *AIAA Journal*, vol. 37, no. 9, pp. 1080–1087, Sep. 1999.
35. Schmisser, J. D., "Receptivity of the Boundary Layer on a Mach-4 Elliptic Cone to Laser-Generated Localized Freestream Perturbations," Doctoral Dissertation, Purdue University Aerospace Sciences Laboratory, December 1997.
36. Holden, M., "Experimental Studies of Laminar, Transitional, and Turbulent Hypersonic Flows Over Elliptic Cones at Angle of Attack," Air Force Office of Scientific Research Technical Report AFRL-SR-BL-TR-98-0142, Bolling Air Force Base, DC, 1998.
37. Schmisser, J. D., Schneider, S. P., and Collicott, S. H., "Response of the Mach 4 Boundary Layer on an Elliptic Cone to Laser-Generated Freestream Perturbations," AIAA Paper 1999-0410, January 1999.
38. Juliano, T., Swanson, E. and Schneider, S.P., "Transition Research and Improved Performance in the Boeing/AFOSR Mach-6 Quiet Tunnel," AIAA Paper 2007-0535, 2007.
39. Choudhari, M., Chang, C.-L., Li, F., Edwards, J., and Candler, G., "Hypersonic Boundary Layer Transition: Roughness Effects and 3D Configurations," NASA Fundamental Aeronautics Program Annual Meeting, Atlanta, GA, Oct. 5-7, 2008.
40. Berger, K., Rufer, S., Kimmel, R., and Adamczak, D., "Aerothermodynamic Characteristics of Boundary Layer Transition and Trip Effectiveness of the HIFiRE Flight 5 Vehicle," AIAA Paper 2009-4055, 2009.
41. Choudhari, M., Chang, C.-L., Li, F., Berger, K., Candler, G., and Kimmel, R., "Transition Analysis for the HIFiRE-5 Vehicle," AIAA Paper 2009-4056, 2009.
42. Berger, K., Rufer, S., Kimmel, R., and Adamczak, D., "Aerothermodynamic Characteristics of Boundary Layer Transition and Trip Effectiveness of the HIFiRE Flight 5 Vehicle," AIAA Paper 2009-4055, 2009.
43. Kimmel, R. A., Adamczak, D., and Juliano, T., "HIFiRE-5 Flight Test Preliminary Results," AIAA Paper 2013-0377, 2013.
44. Paredes, P. and Theofilis, V., "Traveling Global Instabilities on the HIFiRE-5 Elliptic Cone Model Flow," AIAA Paper 2014-0075, 2014.

45. Juliano, T., Adamczak, D., and Kimmel, R. A., "HIFiRE-5 Flight Test Results," *J. Spacecraft and Rockets*, Vol. 52, 2015, pp. 650–663.
46. Juliano, T., Borg, M., and Schneider, S. P., "Quiet Tunnel Measurements of HIFiRE-5 Boundary-Layer Transition," *AIAA J.*, Vol. 53, 2015, pp. 832-84.
47. Borg, M., Kimmel, R. A., and Stanfield, S., "Traveling Crossflow Instability for the HIFiRE-5 Elliptic Cone," *J. Spacecraft and Rockets*, Vol. 52, 2015, pp. 664–673.
48. <http://vulcan-cfd.larc.nasa.gov/index.html> (November 23, 2009)
49. van Albada, G. D., van Leer, B. and Roberts, W. W. , "A Comparative Study of Computational Methods in Cosmic Gas Dynamics," *Astronomy and Astrophysics*, Vol. 108, pp. 76–84, 1982.
50. Edwards, J.R., "A Low-Diffusion Flux-Splitting Scheme for Navier-Stokes Calculations," *Computer and Fluids*, Vol. 6, pp. 635–659, 1997.
51. Litton, D., Edwards, J., and White, J., "Algorithmic Enhancements to the VULCAN Navier-Stokes Solver," AIAA Paper 2003-3979, 2003.
52. Cheatwood, F.M. and Gnoffo, P.A., "User's Manual for the Langley Aerothermodynamic Upwind Relaxation Algorithm (LAURA)," NASA TM 4674, April 1996.
53. Wu, M. and Martin, M. P., "Direct numerical simulation of supersonic boundary layer over a compression ramp," *AIAA Journal*, Vol. 45, No. 4, 2007, pp. 879–889.
54. Jiang, G. S. and Shu, C. W., "Efficient Implementation of Weighted ENO Schemes," *J. Comp. Phys.*, Vol. 126, No. 1, 1996, pp. 202–228.
55. Taylor, E. M., Wu, M., and Martin, M. P., "Optimization of Nonlinear Error Sources for Weighted Non-Oscillatory Methods in Direct Numerical Simulations of Compressible Turbulence," *J. Comp. Phys.*, Vol. 223, No. 1, 2006, pp. 384–397.
56. Williamson, J., "Low-Storage Runge-Kutta Schemes," *J. Comp. Phys.*, Vol. 35, No. 1, 1980, pp. 48–56.
57. Duan, L., Beekman, I., and Martin, M. P., "Direct Numerical Simulation of Hypersonic Turbulent Boundary Layers. Part 3: Effect of Mach Number," *J. Fluid. Mech.*, Vol. 672, 2011, pp. 245–267.
58. Duan, L., Choudhari, M., and Li, F., "Direct Numerical Simulation of Crossflow-Induced Transition in a Swept Wing Boundary Layer," AIAA Paper 2013-2617, 2013.
59. Choudhari, M., Li, F., Duan, L., Carpenter, M. H., Streett, C. L. and Malik, M. R., "Towards Bridging the Gaps in Holistic Transition Prediction via Numerical Simulations," AIAA Paper 2013-2718, 2013.
60. Li, F. and Choudhari, M., "Spatially Developing Secondary Instabilities and Attachment Line Instability in Supersonic Boundary Layers," AIAA Paper 2008-590, 2008.
61. Li, F. and Choudhari, M., "Spatially Developing Secondary Instabilities in Compressible Swept Airfoil Boundary Layers," *Theoretical and Computational Fluid Dynamics*, Vol. 25, pp. 65–84, June,

2011.

62. Paredes, P., Hanifi, A., Theofilis, V., and Henningson, D., "The nonlinear PSE-3D concept for transition prediction in Flows with a Single Slowly-Varying Spatial Direction," *Procedia IUTAM*, Vol. 14C, 2015, pp. 35–44.
63. De Tullio, N., Paredes, P., Sandham, N., and Theofilis, V., "Roughness-induced instability and breakdown to turbulence in a supersonic boundary-layer," *J. Fluid Mech.*, Vol. 735, 2013, pp. 613–646.
64. Li, F., Choudhari, M. M., Carpenter, M. H., Malik, M. R., Chang, C.-L. and Streett, C. L., "Roughness Based Crossflow Transition Control for a Swept Airfoil Design Relevant to Subsonic Transports," AIAA Paper 2010-4380, 2010.
65. Li, F., Choudhari, M., Chang, C.-L., Streett, C. L., and Carpenter, M. H., "Computational Modeling of Roughness-Based Laminar Flow Control on a Subsonic Swept Wing," *AIAA Journal*, Vol. 49, No. 3, 2011, pp. 520-529.
66. Choudhari, M., and Li, F., "Propagation of Instability Waves in Three-Dimensional Boundary Layers," To be submitted for publication as NASA-TM, 2016.
67. Edelman, J., and Schneider, S. P., Private communication, Nov. 2015.
68. Malik, M., Li, F. and Chang, C.-L., "Crossflow Disturbances in Three Dimensional Boundary Layers: Nonlinear Development, Wave Interaction and Secondary Instability," *J. Fluid Mech.*, Vol. 268, pp. 1–36, 1994.
69. White, E. B. and Saric, W. S., "Secondary Instability of Crossflow Vortices," *J. Fluid Mech.*, Vol. 525, Feb. 2005, pp. 275–308.
70. Wassermann, P. and Kloker, M., "Mechanisms and Passive Control of Crossflow Vortex Induced Transition in a Three-Dimensional Boundary Layer," *J. Fluid Mech.*, Vol. 456, April 2002, pp. 49–84.
71. Bonfigli, G. and Kloker, M., "Secondary Instability of Crossflow Vortices: Validation of the Stability Theory by Direct Numerical Simulation," *J. Fluid Mech.*, Vol. 583, July 2007, pp. 229–272.
72. Li, F., Choudhari, M. M., Carpenter, M. H., Malik, M. R., Chang, C.-L., and Streett, C. L., "Roughness Based Crossflow Transition Control for a Swept Airfoil Design Relevant to Subsonic Transports," AIAA Paper 2010-4380, 2010.
73. Li, F., Choudhari, M. M., Carpenter, M. H., Malik, M. R., Chang, C.-L., and Streett, C. L., "Control of Crossflow Transition at High Reynolds Numbers Using Discrete Roughness Elements," To appear in *AIAA Journal*, 2016, doi: 10.2514/1.J054067.
74. Duan, L., Choudhari, M., and Li, F., "Direct Numerical Simulation of Crossflow-Induced Transition in a Swept Wing Boundary Layer," AIAA Paper 2013-2617, 2013.
75. Choudhari, M., Li, F., Duan, L., Carpenter, M. H., Streett, C. L., and Malik, M. R., "Towards Bridging the Gap in Holistic Transition Prediction via Numerical Simulations," AIAA Paper 2013-2718, 2013.

**REPORT DOCUMENTATION PAGE**

*Form Approved  
OMB No. 0704-0188*

The public reporting burden for this collection of information is estimated to average 1 hour per response, including the time for reviewing instructions, searching existing data sources, gathering and maintaining the data needed, and completing and reviewing the collection of information. Send comments regarding this burden estimate or any other aspect of this collection of information, including suggestions for reducing this burden, to Department of Defense, Washington Headquarters Services, Directorate for Information Operations and Reports (0704-0188), 1215 Jefferson Davis Highway, Suite 1204, Arlington, VA 22202-4302. Respondents should be aware that notwithstanding any other provision of law, no person shall be subject to any penalty for failing to comply with a collection of information if it does not display a currently valid OMB control number.  
**PLEASE DO NOT RETURN YOUR FORM TO THE ABOVE ADDRESS.**

<b>1. REPORT DATE (DD-MM-YYYY)</b> 01-12-2015		<b>2. REPORT TYPE</b> Technical Memorandum		<b>3. DATES COVERED (From - To)</b>	
<b>4. TITLE AND SUBTITLE</b>  Secondary Instability of Stationary Crossflow Vortices in Mach 6 Boundary Layer over a Circular Cone				<b>5a. CONTRACT NUMBER</b>	
				<b>5b. GRANT NUMBER</b>	
				<b>5c. PROGRAM ELEMENT NUMBER</b>	
<b>6. AUTHOR(S)</b>  Li, Fei; Choudhari, Meelan M.; Paredes-Gonzalez, Pedro; Duan Lian				<b>5d. PROJECT NUMBER</b>	
				<b>5e. TASK NUMBER</b>	
				<b>5f. WORK UNIT NUMBER</b>  109492.02.07.01.01	
<b>7. PERFORMING ORGANIZATION NAME(S) AND ADDRESS(ES)</b> NASA Langley Research Center Hampton, VA 23681-2199				<b>8. PERFORMING ORGANIZATION REPORT NUMBER</b>  L-20650	
<b>9. SPONSORING/MONITORING AGENCY NAME(S) AND ADDRESS(ES)</b> National Aeronautics and Space Administration Washington, DC 20546-0001				<b>10. SPONSOR/MONITOR'S ACRONYM(S)</b>  NASA	
				<b>11. SPONSOR/MONITOR'S REPORT NUMBER(S)</b>  NASA-TM-2015-218997	
<b>12. DISTRIBUTION/AVAILABILITY STATEMENT</b> Unclassified - Unlimited Subject Category 01 Availability: NASA STI Program (757) 864-9658					
<b>13. SUPPLEMENTARY NOTES</b>					
<b>14. ABSTRACT</b> Hypersonic boundary layer flows over a circular cone at moderate incidence can support strong crossflow instability. Due to more efficient excitation of stationary crossflow vortices by surface roughness, such boundary layer flows may transition to turbulence via rapid amplification of the high-frequency secondary instabilities of finite amplitude stationary crossflow vortices. The amplification characteristics of these secondary instabilities are investigated for crossflow vortices generated by an azimuthally periodic array of roughness elements over a 7-degree half-angle circular cone in a Mach 6 free stream. Depending on the local amplitude of the stationary crossflow mode, the most unstable secondary disturbances either originate from the second (i.e., Mack) mode instabilities of the unperturbed boundary layer or correspond to genuine secondary instabilities that reduce to stable disturbances at sufficiently small amplitudes of the stationary crossflow vortex. The predicted frequencies of dominant secondary disturbances are similar to those measured during wind tunnel experiments at Purdue University and the Technical University of Braunschweig, Germany.					
<b>15. SUBJECT TERMS</b>  Boundary layer flow; Circular cones; Cross flow; Stability; Vortices					
<b>16. SECURITY CLASSIFICATION OF:</b>			<b>17. LIMITATION OF ABSTRACT</b>	<b>18. NUMBER OF PAGES</b>	<b>19a. NAME OF RESPONSIBLE PERSON</b>
<b>a. REPORT</b>	<b>b. ABSTRACT</b>	<b>c. THIS PAGE</b>			STI Help Desk (email: help@sti.nasa.gov)
U	U	U	UU	29	<b>19b. TELEPHONE NUMBER (Include area code)</b>  (757) 864-9658